ETH
Eidgenössische Technische Hochschule Zürich
Swiss Federal Institute of Technology Zurich

IGP
Institut für Geodäsie und
Photogrammetrie

Interdisciplinary Project

Satellite-Independent Embedding Learning for Lake Ice Monitoring

Autumn Term 2020

Supervised by:
Manu Tom (PRS), Prof. Konrad Schindler (PRS),
Prof. Fabian Walter (VAW)

Author:
Yuchang Jiang

Contents

List of Figures

List of Tables

Abstract

Lake ice is an Essential Climate Variable (ECV) to study climate change. For lake ice monitoring, two dates, ice-on and ice-off date, are of particular interest. The previous studies in this field have proven the usefulness of using satellite data sources like Moderate Resolution Imaging Spectroradiometer (MODIS), Visible Infrared Imaging Radiometer Suite (VIIRS) , Sentinel-1 Synthetic Aperture Radar (SAR) to monitor lake ice. As each satellite data source has its own advantages and disadvantages, a possible but challenging way of improvement is data fusion. Main challenges of data fusion are large spatial resolution difference and domain gap between various remote sensing images.

This exploration work applies the idea of embedding learning to fuse three satellite data sources, MODIS, VIIRS and Sentinel-1 SAR with fours lakes in Switzerland as the region of interest. A variant of Deeplab v3+ is created to achieve optical-SAR fusion and obtain embedding. To apply the learnt embedding for ice-on and ice-off date determination, two different models are tried: 2-step model and end-to-end model. The results indicate 2-step model can produce more accurate ice-on and ice-off date comparing to end-to-end model and other previous methods. For three large lakes, the accuracy of dates predicted by 2-step model is around 3 days while the accuracy of one small lake is more than a week.

Keywords: lake ice monitoring, convolutional neural network, embedding learning, data fusion, domain adaptation

Acknowledgement

I would like to thank:

- **Manu Tom** for the instruction and help throughout the project
- **Prof. Dr. Konrad Schindler** for giving guidance during the project
- **Roberto Aguilar** and **Tianyu Wu** for helping me understand data preprocessing step in the previous works

Chapter 1

Introduction

Climate change is a main challenge facing humanity, which requires rapid effort [1]. To understand the evolution of climate change and provide guidance, Essential Climate Variables (ECVs) are observed and investigated, according to the Global Climate Observing System (GCOS) Climate Monitoring Principles. [2]. 'Lakes' is recognised as an ECV and the related products include lake ice cover so lake ice monitoring is important for research about climate change. Besides, considering the role of lake ice in winter activities, the economic and social values of lake ice also underline the importance of lake ice monitoring.

From [3], there are two important dates for lake ice monitoring: one is 'ice-on' date, which is the first day when lake is completely frozen and the other one is 'ice-off' date, the first day when lake is completely liquid water. Based on these two dates, the freezing pattern of a lake can be observed and defined. The accuracy requirement defined by GCOS for ice-on and ice-ff date is ± 2 days [4]. In the previous works of lake ice monitoring, remote sensing images are main data sources to detect lake ice and determine these two dates. In 2018, Tom et al. used MODIS and VIIRS to monitor lake ice for lakes in Switzerland [5] and recently Sentinel-1 SAR images are used to detect lake ice for lakes in alpine environment [4]. For optical images like MODIS and VIIRS, they have good temporal resolution (almost daily acquisition) but poor spatial resolution, for example, 250m for some spectral bands of MODIS. Besides, optical images suffer from cloud problem, which reduces the number of useful pixels. On the other hand, Sentinel-1 SAR can penetrate cloud and have better spatial resolution, 10m but the temporal resolution is worse than MODIS and VIIRS. Because of their limitations, it is still hard for the previous lake ice monitoring system using MODIS, VIIRS or Sentinel-1 SAR to fulfill the accuracy requirement defined by GCOS.

To improve the accuracy of prediction of ice-on and ice-off date, one possible way is to fuse different satellite images to combine their advantages. However, there are many challenges for data fusion in remote sensing field. To fuse optical images (MODIS and VIIRS) and SAR images (Sentinel-1) used in the previous works, one main challenge is the large domain gap. It is hard to bridge the domain gap between optical and SAR domain. Besides, how to fuse data with large spatial resolution difference is another challenge: the spatial resolution of VIIRS, 375m is much larger than that of Sentinel-1 SAR, 10m. Therefore, combining various satellite data sources to improve the accuracy in lake ice monitoring is a possible but challenging solution.

Here this work aims to fuse different satellite data (MODIS, VIIRS, Sentinel-1 SAR)

by embedding learning. Through embedding learning, three satellite data sources are fused together. The embedding learning task will be considered as a supervised segmentation problem and the model is based on Deeplab v3+ [6]. The developed embedding will be applied to predict the portion of water of the lake, from which ice-on and ice-off dates are extracted for four lakes in two winters in Switzerland. These extracted dates can be used to analyze the freezing pattern of lakes.

This report will firstly introduce related work including lake ice monitoring, data fusion and domain adaptation in Section 2. Then selected data and data preprocessing methods are discussed in Section 3. After introducing data, models implemented are explained in Section 4 and experiment results are discussed in Section 5. Finally, conclusion of the whole work is shown in Section 6.

Chapter 2

Related Work

2.0.1 Lake Ice Monitoring

The literature of lake ice monitoring is vast. For dataset, the majority of existing works used satellite images. Latifovic and Pouliot extracted four important dates (break-up start, break-up end, freeze-up start, freeze-up end dates) to define the freezing pattern of Canadian lakes with the data of Advanced Very High Resolution Radiometer (AVHRR) sensor in order to analyze climate change in long time series [7]. Tom et al. applied Support Vector Machine (SVM) on MODIS and VIIRS satellite images to perform lake ice detection for lakes in Switzerland [5]. Duguay and Lafleur used Landsat Thematic Mapper (TM) and European Remote Sensing (ERS)-1 SAR images to observe depth and ice thickness of lakes [8]. Then in the last year, Tsai et al. used Sentinel-1 SAR images to detect web and dry snow for mountainous areas [9]. Recently Sentinel-1 SAR images are trained with a deep learning model (Deeplab v3+) to perform lake ice detection for lakes in Switzerland [4]. Besides satellite images, other image sources like webcam images also play a role in lake ice monitoring tasks. Xiao et al. proposed an encoder-decoder neural network model to achieve segmentation on webcam images for lake ice monitoring [10]. Then Prabha et al. implemented a Deep-U-Lab, a variant from Deeplab v3+ [6] to improve the performance of webcam images and showed the possibility of using other crowd-sourced images on lake ice monitoring [11].

Previous works demonstrate that there is a diversity of dataset and methods used in lake ice monitoring tasks. For dataset, although the majority used satellite images, there is a recent trend for other sources like webcam images. Each dataset may have its own advantages and disadvantages. For optical satellite images like MODIS and VIIRS, they have nearly daily temporal resolution but poor spatial resolution (for example, 250m for some spectral bands of MODIS). Besides, optical images suffer from cloud problem, which reduces the number of useful pixels further. For SAR images, they can avoid cloud problem but have worse temporal resolution than optical images. For webcam or crowd-source images, they are only available for some certain lakes and it is hard to configure those public cameras. As for methods, the traditional methods like SVM are widely used while deep learning methods like convolutional neural network are getting more and more attentions. Therefore, it would be nice if we can benefit from data fusion and leverage state-of-art deep learning methods.

2.0.2 Data Fusion in Remote Sensing

Data fusion has been a popular topic in remote sensing field for decades. The traditional data fusion in remote sensing tries to combine high-resolution panchromatic band and low-resolution multispectral bands (pansharpening). This includes methods like Brovey transformation and principal component substation [12]. Besides, spatiotemporal fusion is an increasing trend to achieve high spatial and temporal resolution. [13]. Song et al. applied convolution neural network to combine the spatial information of Landsat images with the temporal information of MODIS image [14]. Besides fusing two optical image sources, there is also a trend to fuse different kinds of remote sensing images. Last year Feng et al. created a two-branch neural network in which one branch could extract features from hyperspectral images and the other branch could extract features from Light Detection and Ranging (LiDAR) data [15]. Then features are combined to predict labels for urban land-use mapping. Recently Hughes et al. proposed a three-step deep learning framework to combine optical and SAR images, which could improve the accuracy of geo-localization for optical images [16]. Based on previous methods, it is possible to fuse different kinds of satellite images and deep learning seems to be the start-of-art method for data fusion as it is able to capture high-level features and make decisions. To achieve data fusion in this work, we would like to explore the possibility of using embedding learning, a common idea in Natural Language Processing tasks, in the field of remote sensing.

2.0.3 Domain Adaptation

Domain adaptation can capture transferable representation or embedding by deep learning network [17]. Thus, it can be a strategy to solve the problem of the lack of labeled data and also be applied to data fusion. Classic domain adaption includes fine-tuning or modifying model trained on source data with target data and using metrics to capture the discrepancy between source and target data distribution [18]. On the other hand, deep domain adaptation tries to narrow the domain gap by optimizing the architecture of deep neural network, which usually involves 'weight-sharing' or 'weight-related' idea. Recent works have proven the effectiveness of deep domain adaptation. Chopra et al. employed a Siamese network for weight sharing and feature extraction to perform domain adaption [19]. Then Lv et al. used weight-sharing convolutional layers in a deep learning network to extract features from source and target images for semantic segmentation task [20]. Instead of weight-sharing, Rozantsev et al. used weight-related idea: there is a loss function to minimize the difference of weights in blocks for source and target images [18]. As weight-sharing and weight-related idea are proven to be useful in domain adaption, this work will try to use similar idea in the field of remote sensing data fusion.

Chapter 3

Data

3.0.1 Target lakes

To monitor lake ice, four lakes in Switzerland, lake Sihl, Sils, Silvaplana and St.Moritz are chosen. From Figure 3.1, three lakes, Sils, Silvaplana, St Moritz are closer to each other and may have similar environment while lake Sihl is far away from others. Besides, lake Sihl is an artificial lake. It is created by damming river Sihl and flooding section of nearby valley. As shown in Table 3.1, those lakes have different altitude, area size and depth. Therefore, the diversity of lakes in our data can help test the generalisation of developed model. For each lake, we have the satellite data (MODIS, VIIRS and Sentinel-1 SAR) for two winters, winter 2016-17 and winter 2017-18.

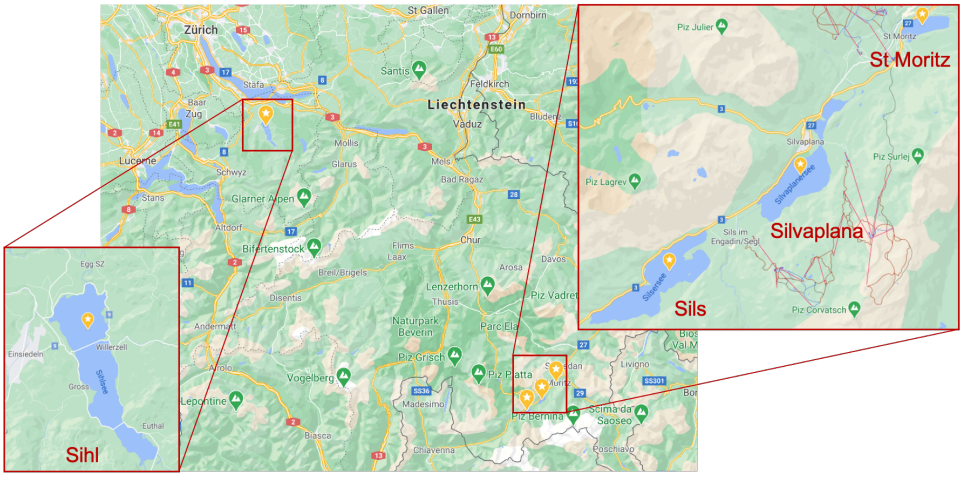

Figure 3.1: Geographic locations of lakes

Table 3.1: Summary of chosen lakes

Chosen Lakes				
	Sihl	Sils	Silvaplana	St.Moritz
Area(km^2)	11.3	4.1	2.7	0.78
Altitude(m)	889	1797	1791	1768
Max.Depth(m)	17	71	77	42
Volume(Mm^3)	96	137	140	20

3.0.2 Optical Images (MODIS and VIIRS)

MODIS and VIIRS data for four lakes in two winters are chosen and preprocessed with the same preprocessing procedure as introduced in [5], which includes georeferencing, absolute location correction, cloud filtering and bilinear interpolation for low-resolution bands (for example, upsample 500m band to 250m for MODIS). All cloud-free lake pixels in the acquisition with more than 30% non-cloud coverage are extracted. After processing, there is no VIIRS data for lake St.Moritz. Because the area size of lake St.Moritz is only $0.78km^2$ and the spatial resolution of VIIRS is $375m$, there is no pixel full of lake can be extracted. As for band selection, instead of using all available bands, 12 out of 36 spectral bands are selected for MODIS and 5 out of 22 spectral bands are selected for VIIRS data as suggested by [5]. To form image with uniform size, lake pixels are padded with background pixels to form 12x12 image size for each channel. Therefore, the size of preprocessed MODIS image is 12x12x12 and the size of preprocessed VIIRS image is 12x12x5. The summary of optical images is displayed in Table 3.2.

3.0.3 SAR Images (Sentinel-1 SAR)

Sentinel-1 SAR data for four lakes in two winters are chosen and are preprocessed with the same preprocessing methods as stated in [4], which includes border noise removal, thermal noise removal, radiometric calibration, terrain correction, log scaling and cropping to 128∗128 size. Although there are four polarisation for Sentinel-1 SAR, only VV and VH polarisation are available for the region of interest so the final image size of Sentinel-1 is $128 * 128 * 2$. The summary of Sentinel-1 images is displayed in Table 3.2.

Table 3.2: Summary of data

Data			
	MODIS	VIIRS	Sentinel-1
Satellite Type	Optical	Optical	SAR
Spatial Resolution	250m	375m	10m
Temporal Resolution	1d	1d	2-3d
No. Channel	12(36)	5(22)	2(4)
Cloud Problem	Yes	Yes	No

3.0.4 Ground Truth

There are three sources of ground truth data in this work: per-pixel segmentation ground truth, per-day label of lake condition, ice-on and ice-off date of lake.

For per-pixel segmentation ground truth, there are three classes: frozen, nonfrozen and background (or no-lake). They are labeled by human operator for all three satellite data. However, due to the difficulty of labeling pixels in transition period (when lake is a mixture of water and ice), only data in non-transition period (when lake is totally frozen or totally liquid water) are available.

For per-day label of lake condition, human operators annotated the ground truth by observing available webcam data with one of nine possible labels: snow, ice, water, more snow, more ice, more water, clouds, unclear, no data. For practical use, these text labels are converted into numeric values to represent the portion of water: convert 'snow' and 'ice' to 0, 'more snow' and 'more ice' to 0.25, 'more water' to 0.75 and 'water' to 1. For days with uncertain labels like 'clouds', 'unclear' or 'no data' labels, we replace it with the label of the closest day, if valid ground truth

exists for that day.

For ice-on and ice-off date, they are based on visual interpretation of human operators. These ground truth data are downloaded from the open source repository of previous work [4] (https://github.com/czarmanu/sentinel_lakeice/tree/master/data/gt). The ground truth data are available for all four lakes in winter 2016-17.

Chapter 4

Methodologies

Methodologies are divided into two parts:

1. Achieve embedding learning with a segmentation model
2. Apply embedding to a specific task: the prediction of the nonfrozen (liquid water) portion of lake

4.0.1 Embedding Learning

Deeplab v3+

Deeplab v3+ is proved to be a promising model for semantic segmentation tasks [6]. As shown in Figure 4.1, Deeplab v3+ leverages atrous convolution to capture information at different scales and combine the low-level features with high-level features. As suggested by [4], Deeplab v3+ is a good choice for lake ice monitoring tasks with Sentinel-1 data. Therefore, we used Deeplab v3+ to train Sentinel-1 SAR data and the loss function used here is cross entropy loss function.

General parameter settings: epoch number is 100, batch size is 16, optimizer is Adam [21], learning rate is 0.0001, use pretrained MobileNetV2 [22] on ImageNet [23] as backbone, set 1, 2, 3 as rate for atrous convolution.

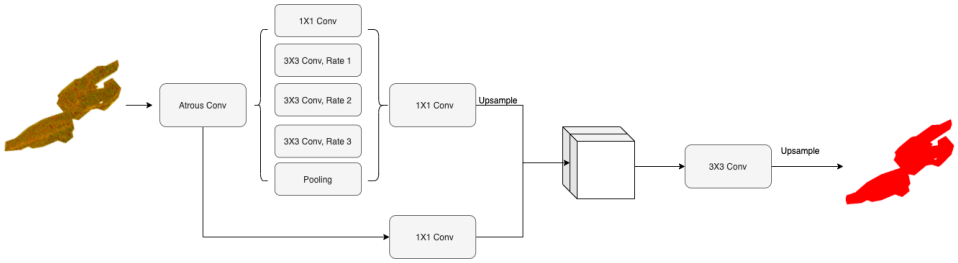

Figure 4.1: Network structure of Deeplab v3+

Optical-Optical Fusion

Because MODIS and VIIRS have poor spatial resolution, it is not suitable for deep network structure. Thus, a shallow network with 1x1 convolutional layers are designed to fuse them. As Figure 4.2 shows, different encoders are used for MODIS and VIIRS and one shared block is used for weight sharing and combination. Each

encoder is one 1x1 convolution layer. The shared block consists of several 1x1 convolution layers and concatenation layers. With encoders and shared block, the feature layer (green block) with 12x12x32 size can be treated as learnt embedding. The loss function used here is cross entropy loss function.

General parameter settings: epoch number is 5-10 for MODIS and VIIRS, batch size is 8, optimizer is Adam [21], learning rate is 0.0005.

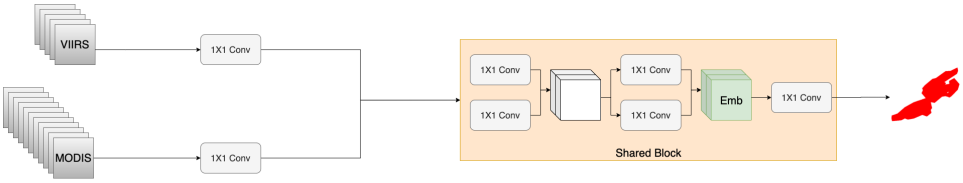

Figure 4.2: Network structure of fusion model (optical-optical)

Optical-SAR Fusion

With pretrained optical-optical fusion model and Deeplab v3+ model, the encoder of Deeplab v3+ can be combined with optical-optical fusion model to form optical-SAR fusion model, which means each component of optical-SAR fusion model is already pretrained. The overall network structure of this optical-SAR fusion is depicted in Figure 4.3. Because the last layer of standard Deeplab v3+ is an upsample layer to preserve the resolution of input images (as shown in Figure 4.1), one upsample layer is added in the end of optical-SAR fusion model if inputs are Sentinel-1 SAR images. This will not affect the training of model as there is no trainable parameters in upsample layer. Although the image size segmentation result is different for three data sources, it is not a problem for this fusion model: convolutional layers can take images with different size as input.

The whole training process of this fusion model includes two stages: the first one is to pretrain Deeplab v3+ on Sentinel-1 SAR and pretrain optical-optical fusion on MODIS and VIIRS; the second stage is fine-tuning. The main reason of fine-tuning is to make shared block be compatible with both optical and SAR images. To fine tune the optical-SAR fusion model, Sentinel-1 data are used to go through this model, which includes the joint training of the encoder of Deeplab v3+ and main shared block. During this process, the first 82 layers of the encoder of Deeplab v3+ are frozen as the extraction of low-level features should be unaffected. After fine tuning, the feature layer (green block in Figure 4.3) can be treated as learnt embedding. The loss function used here is cross entropy loss function.

General parameter settings: epoch number is 20, batch size is 16, optimizer is Adam [21], learning rate is 0.0001.

4.0.2 Application of Learnt Embedding

2-Step Model

2-step model consists of two steps:

1. use the mentioned segmentation model (optical-SAR fusion model) to learn embedding

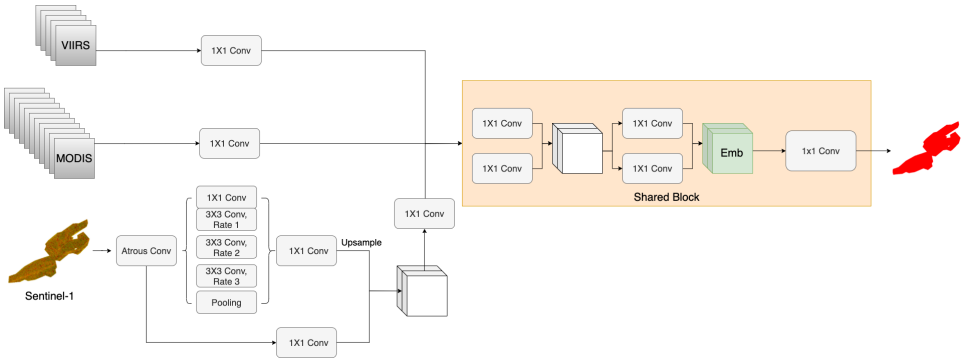

Figure 4.3: Network structure of fusion model (optical-SAR)

2. use learnt embedding to predict the portion of water in the lake with a regression model

As depicted in Figure 4.4, the first step is the same as optical-SAR fusion. Because the size of optical and SAR images are different, the size of embedding of SAR images is larger than that of optical images. Thus, one post-processing step is to resize the embedding of SAR images to ensure uniform embedding size. Then the learnt embedding (the green block) is stacked along time dimension to leverage temporal information. For example, the embedding from yesterday, current day and the day after are stacked together and feed into the second step, a regression model, which will output the portion of water of a lake. Here we use 'timestep' to denote the number of embedding stacked along time dimension so for the example mentioned before, the timestep is 3. In regression model, the top four layers are convolution layers operated on each time dimension followed by a reshape layer (in order to reduce time dimension). Before this reshape layer, the dimension of feature layer is (batch size, timestep, image width, image height, channel size). After the reshape layer, the dimension of feature layer becomes (batch size, image width, image height, timestep * channel size). Then three convolution layers are performed on the reshaped features followed by a fully connected layer. The detailed network structure is summarized in Figure 4.5. For step 1, we still use cross entropy as loss function. As for step 2, the following loss function is used:

$$L_{reg} = L_{MSE} + \alpha L_{line} + \beta L_{nms} \tag{4.1}$$

L_{MSE}: Mean Squared Error
L_{line}: fit predictions of neighboring days to a simple straight line $(kx + b)$ and compute the orthogonal distance between each prediction to the straight line. It can act as a smooth function to suppress noises for the final time series plot. The detailed computation is as the following formula:

Simple line fitting in a batch:

$$k = \frac{y_{pred}^{last} - y_{pred}^{first}}{batch\ size}, \quad b = y_{pred}^{first} \tag{4.2}$$

Orthogonal distance computation of the i-th prediction in a batch:

$$distance^i = \frac{|ki + b - y_{pred}^i|}{\sqrt{k^2 + 1}} \tag{4.3}$$

L_{nms}: compute the variance of predictions from the same day to perform non-maximum suppression. As different satellite sources are combined, it is possible to

have more than one acquisition for one day. This loss can minimize the differences between those predictions from the same day.

General parameter settings: The settings for step 1 is the same as that of optical-SAR fusion. For step 2, time dimension is 7, epoch number is 30, batch size is 8, optimizer is Adam [21], learning rate is 0.0005, α and β are 0.08.

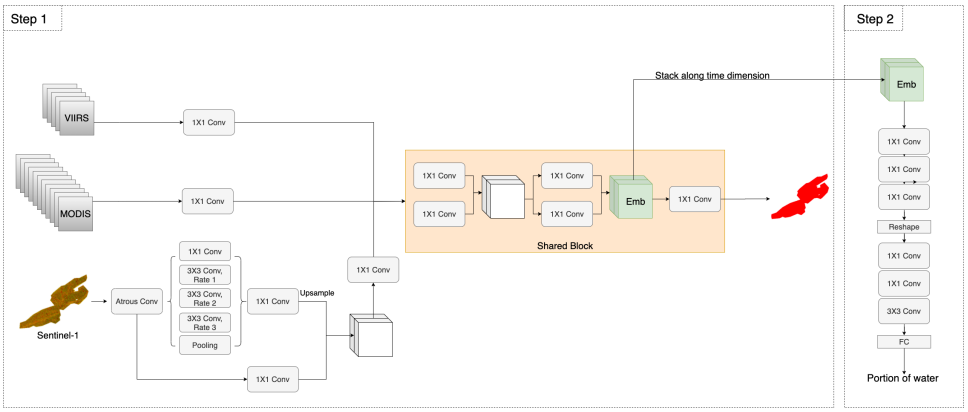

Figure 4.4: Network structure of 2-step model

Layer (type)	Output Shape	Param #
time_distributed_4 (TimeDist	multiple	396
time_distributed_5 (TimeDist	multiple	104
time_distributed_6 (TimeDist	multiple	27
reshape (Reshape)	multiple	0
conv2d_12 (Conv2D)	multiple	704
conv2d_13 (Conv2D)	multiple	528
conv2d_14 (Conv2D)	multiple	1160
flatten_1 (Flatten)	multiple	0
dropout (Dropout)	multiple	0
dense_1 (Dense)	multiple	801

Total params: 3,720
Trainable params: 3,720
Non-trainable params: 0

Figure 4.5: Details of structure of regression model

End-to-End Model

Instead of treating embedding learning and task solving as two separated steps, end-to-end model tries to combine them into a two-branch model. This end-to-end model consists of two branches:

1. use segmentation model (optical-SAR fusion model) as segmentation branch to guide embedding learning
2. use regression model (same as the second step in 2-step model) to guide embedding learning and obtain the portion of water in the lake simultaneously

As shown in Figure 4.6, the previous step 1 (segmentation model) becomes the segmentation branch while the step 2 (regression model) becomes the other branch.

The network structure of each branch is the same as the corresponding step in Figure 4.4. The training process of end-to-end consists of pretraining and joint training stages. In pretraining stage, optical-optical fusion model and Deeplab v3+ are pretrained. Then in joint training stage, all satellite images are feed into end-to-end model. During joint training, the first 82 layers of Deeplab v3+ are frozen as the low-level feature extraction will remain the same. For the joint training, the loss function is defined as:

$$L_{e2e} = w_1 L_{seg} + w_2 L_{reg} + w_3 L_{con} \tag{4.4}$$

L_{seg}: cross entropy loss
L_{reg}: as defined in Equation 4.1
L_{con}: compute the absolute difference between prediction from the regression branch and the portion of water calculated from segmentation result:

$$portion = \frac{\#nonfrozen\ pixels}{\#lake\ pixels} \tag{4.5}$$

General parameter settings: The segmentation part of end-to-end model consists of pretrained optical-optical model, the encoder of Deeplab v3+ and the shared block. The pretraining process uses the same parameter setting as the settings mentioned in Deeplab v3+ and optical-optical fusion part. As for joint training, time dimension is 7, epoch number is 10, batch size is 8, optimizer is Adam [21], learning rate is 0.0001, α is 0.25, β is 0.05, w_1 and w_2 are 0.5 and w_3 is 1.

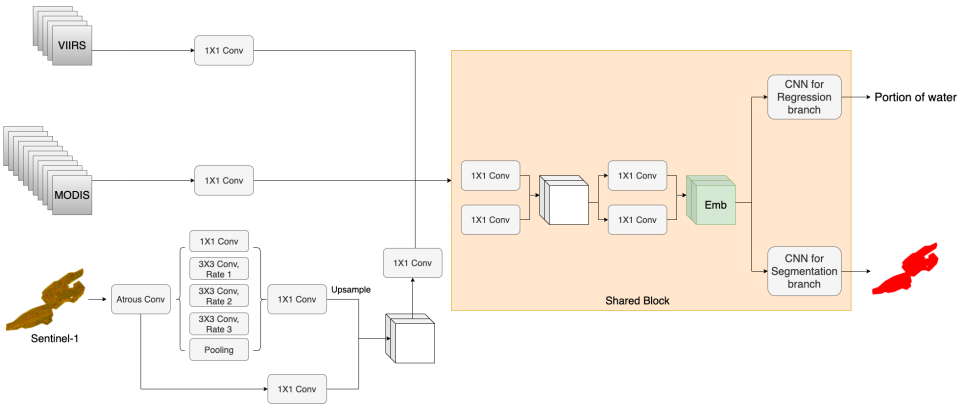

Figure 4.6: Network structure of end-to-end model

Chapter 5

Experiments & Results

To check the performance of models, usually data are split into training and testing set by some portion for experiment, for example, 75% for training and 25% for testing. However, we need to keep data completeness for each lake in order to generate complete time series plot and extract ice-on/off date. Therefore, instead of splitting data randomly, 'Leave-One-Out' setting is used in experiments. Here the 'Leave-One-Out' means leave one winter or leave one lake. For example, leave winter 2016-17 experiment means training on the data of all lakes in winter 2017-18 and testing on the data of all lakes in winter 2016-17. Those segmentation models (Deeplab v3+, optical-optical fusion, optical-SAR fusion) are trained on data from non-transition period as segmentation ground truth from transition period is not available. We use accuracy and mean Intersection-over-Union (mIoU) to check the performance of segmentation models. As for 2-step model and end-to-end model, the segmentation parts are pretrained on data from non-transition part but all data from non-transition and transition period are used to generate embedding, which means when generating embedding in training stage, data from transition period will not be counted for loss computation. Then regression part will take data from both periods. To check the performance of 2-step and end-to-end model, we conduct rough visual checking on time series plots as there is no suitable metric available.

The reported results include quantitative and qualitative measurements. For quantitative measurements, accuracy and mIoU are used as segmentation metrics. For qualitative checking, we focus on the visualization of embedding and time series plot of predicted portion of water. To compare with previous related works, ice-on and ice-off dates are extracted and discussed.

5.0.1 Quantitative Result of Segmentation

To check the stability of models, all leave-one-out experiments (two leave-one-winter-out and four leave-one-lake-out experiments) are performed for segmentation models including Deeplab v3+ on Sentinel-1 SAR, optical-optical fusion on MODIS, VIIRS and optical-SAR fusion on all satellite images. The results of segmentation using separated models for optical images and SAR images are shown in Table 5.1 and Table 5.2. The results of segmentation of optical-SAR fusion are displayed in Table 5.3 and Table 5.4. Comparing the results of separated models (Deeplab v3+ and optical-optical fusion) with that of optical-SAR fusion, both accuracy and mIoU are similar so the data fusion is successful with aspect to segmentation. As optical-SAR fusion is directly used as the first step in 2-step model, it also suggests the segmentation part of 2-step model is successful. For the segmentation branch

of end-to-end model, results are shown in Table 5.5 and Table 5.6. Comparing the results of 2-step model and end-to-end model, it seems end-to-end model performs slightly better than 2-step model. As the final objective is to narrow the domain gap and obtain embedding instead of semantic segmentation, a better result of segmentation does not mean end-to-end model is superior. A more detailed investigation is required for learnt embedding.

Table 5.1: Results of separated training of optical (optical-optical model) and SAR images (Deeplab v3+) on Leave-one-winter experiments

Image Source	winter 16		winter 17	
	accuracy	mIoU	accuracy	mIoU
MODIS	96.57%	82.72%	97.55%	85.96%
VIIRS	98.75%	87.46%	98.79%	86.16%
Sentinel-1	94.42%	75.14%%	95.90%	80.92%

Table 5.2: Results of separated training of optical (optical-optical model) and SAR images (Deeplab v3+) on leave-one-lake experiments

Image Source	Sihl		Sils		Silvaplana		St.Moritz	
	accuracy	mIoU	accuracy	mIoU	accuracy	mIoU	accuracy	mIoU
MODIS	97.90%	73.54%	99.38%	89.21%	97.57%	82.17%	99.79%	81.93%
VIIRS	89.10%	84.73%	95.19%	78.64%	98.47%	72.20%	-	-
Sentinel-1	94.49%	61.84%%	96.20%	82.97%	95.04%	79.85%	95.36%	76.45%

Table 5.3: Results of optical-SAR fusion (or 2-step model) on leave-one-winter experiments

Image Source	winter 16		winter 17	
	accuracy	mIoU	accuracy	mIoU
MODIS	96.62%	83.65%	96.64%	81.62%
VIIRS	98.75%	87.95%	99.07%	87.76%
Sentinel-1	95.04%	78.51%	94.89%	78.20%

Table 5.4: Results of optical-SAR fusion (or 2-step model) on leave-one-lake experiments

Image Source	Sihl		Sils		Silvaplana		St.Moritz	
	accuracy	mIoU	accuracy	mIoU	accuracy	mIoU	accuracy	mIoU
MODIS	93.32%	81.40%	98.34%	89.61%	97.70%	83.09%	99.78%	82.33%
VIIRS	98.16%	86.41%	99.35%	89.35%	99.41%	88.50%	-	-
Sentinel-1	94.24%	62.22%	94.91%	79.69%	94.85%	80.17%	94.39%	74.14%

Table 5.5: Results of end-to-end model on leave-one-winter experiments

Image Source	winter 16		winter 17	
	accuracy	mIoU	accuracy	mIoU
MODIS	96.99%	85.32%	97.19%	84.22%
VIIRS	99.05%	91.57%	99.31%	90.37%
Sentinel-1	96.43%	84.32%	92.93%	74.60%

Table 5.6: Results of end-to-end model on leave-one-lake experiments

Image Source	Sihl		Sils		Silvaplana		St.Moritz	
	accuracy	mIoU	accuracy	mIoU	accuracy	mIoU	accuracy	mIoU
MODIS	92.88%	80.55%	93.07%	80.59%	98.50%	90.64%	99.77%	87.18%
VIIRS	97.50%	84.34%	97.79%	85.46%	99.62%	94.29%	-	-
Sentinel-1	91.07%	64.21%	89.26%	61.70%	94.46%	80.01%	94.56%	77.89%

5.0.2 Qualitative Visualization of Embedding

As we use segmentation model to achieve embedding learning task, checking the visualization of embedding is important. After performing dimension reduction with t-distributed Stochastic Neighbor Embedding (t-SNE) [24], the embedding from two models, 2-step model and end-to-end are displayed in Figure 5.1. Here we chose t-SNE instead of Principle Component Analysis (PCA) as t-SNE is better to preserve the neighboring relationship. With t-SNE, we can have a rough idea about which embedding are clustered in the high-dimensional space. In Figure 5.1, the embedding resulted from 2-step model look reasonable: they are clustered by colors, which represent the portion of water in the lake. As for the result of end-to-end model, the embedding are not clustered by colors but by something else. To investigate this problem, we use satellite type to represent the symbol shape of embedding. The result of Lake Silvaplana in winter 2016-17 from end-to-end model is shown in Figure 5.2, in which MODIS, VIIR, Sentinel-1 SAR are in round, square and diamond shape. It is obvious that embedding are clustered by satellite type so the domain gap is still large in the result of end-to-end model. Comparing the result of these two models, 2-step model can narrow the domain gap better. As 2-step model only uses segmentation while end-to-end model combines segmentation and regression to guide embedding learning, the results suggest segmentation model can perform embedding learning better than the joint learning of segmentation and regression. However, although embedding learnt by 2-step model is better, we can still notice some domain gaps, especially in leave winter 2017-18 experiment. To summarize, there is still large space for investigation and improvement for embedding learning.

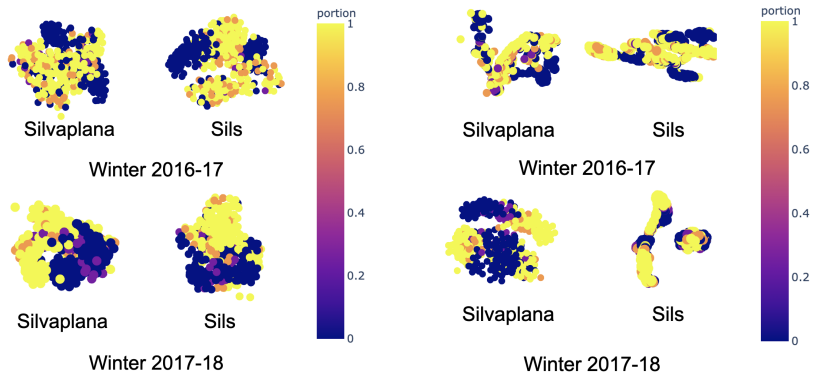

((a)) Embedding from 2-step model

((b)) Embedding from end-to-end model

Figure 5.1: Embedding from leave winter 2016-17 experiment and leave winter 2017-18 experiment

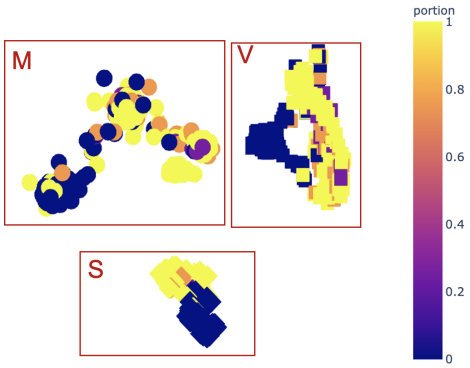

Figure 5.2: Zoomed-in visualization of embedding learnt by end-to-end model for Lake Silvaplana in winter 2016-17 in leave winter 2016-17 experiment

5.0.3 Qualitative Result of Time Series Plot

From both 2-step model and end-to-end model, daily predictions of the portion of water are obtained for each lake. To check the performance, leave winter 2016-17 experiment is conducted on both models. These predictions can form the time series plots in Figure 5.3 and 5.4. In time series plots, ground truth based on visual interpretation of human operator is shown as blue line and predictions from different months are shown as points with different colors. From Figure 5.3, the result of 2-step model is close to ground truth, especially in non-transition period. Because we only have non-transition training data for embedding learning, it is 'unsupervised' and hard to predict the portion of water in transition period. In general, the result of 2-step model captures the general trend of ground truth and the corner points (for example, ice-on and ice-off dates) are clear. Among results of all four lakes, time series plot of lake St.Moritz is not as good as others. Considering the small area size of this lake, the imbalance of data may cause the generalisation problem of 2-step model. As for the result of end-to-end model in Figure 5.4, it is more noisy and many predictions are deviated from ground truth. Because the embedding learning of end-to-end is worse than 2-step model, it indicates the successful embedding learning and narrowed domain gap are essential for an accurate time series plot.

5.0.4 Quantitative Result of Ice-on and Ice-off Dates

Ice-on and ice-off dates are important for lake ice monitoring. Based on daily predictions of portion of water, ice-on and ice-off dates are extracted. Regression tree is used to fit predictions and split them into intervals: water period, freezing period, frozen period, melting period and water period. Then the end of freezing period is considered as ice-on date and the end of melting period is considered as ice-off date. The results of ice-on and ice-off dates in winter 2016-17 from different methods are summarized in Table 5.7. Two columns in blue (2-Step and E2E) are results of 2-step model and end-to-end model. GT is the ground truth based on visual interpretation by human operator. There are two methods from previous works: 'M+V' means a combination of MODIS and VIIRS prediction results with Support Vector Machine (SVM) and 'Webcam' means the prediction results of using neural network on webcam images [25]. By comparing results from different methods to ground truth, 2-step model slightly outperforms other methods: for lake Sihl, lake Sils and lake Silvaplana, 2-step model can produce better results than end-to-end model and other previous methods. Comparing predicted dates of four lakes, the predictions of lake Sihl and lake Sils are more accurate than other. This is because

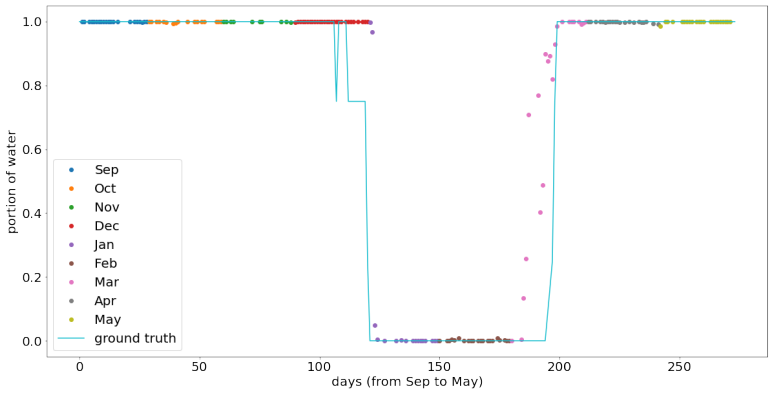

((a)) Lake Sihl in winter 2016-17

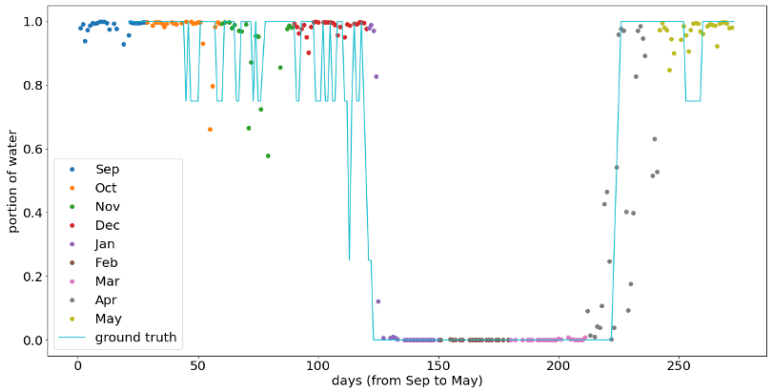

((b)) Lake Sils in winter 2016-17

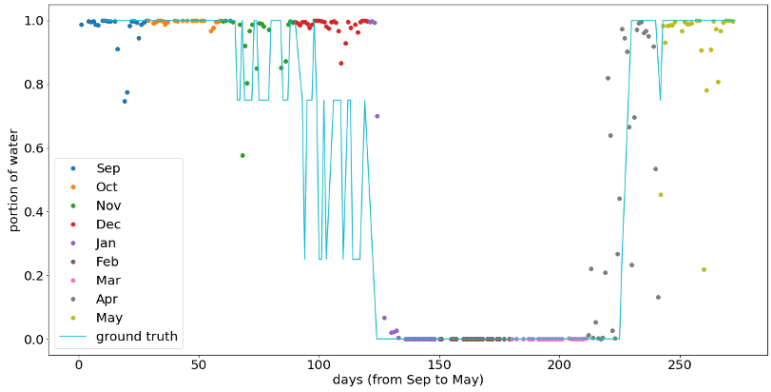

((c)) Lake Silvaplana in winter 2016-17

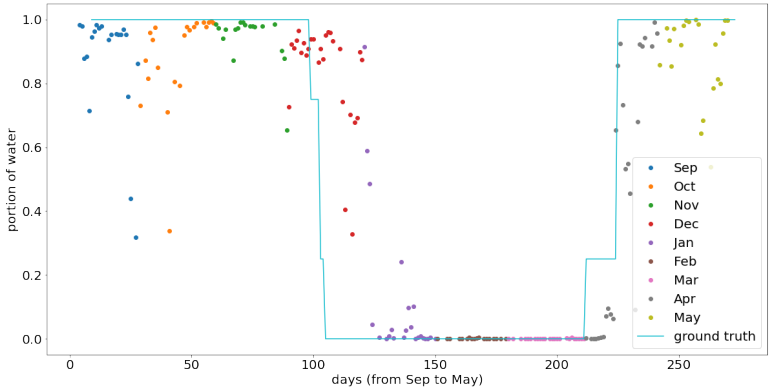

((d)) Lake St.Moritz in winter 2016-17

Figure 5.3: Time series plot of 2-step model from leave winter 2016-17 experiment

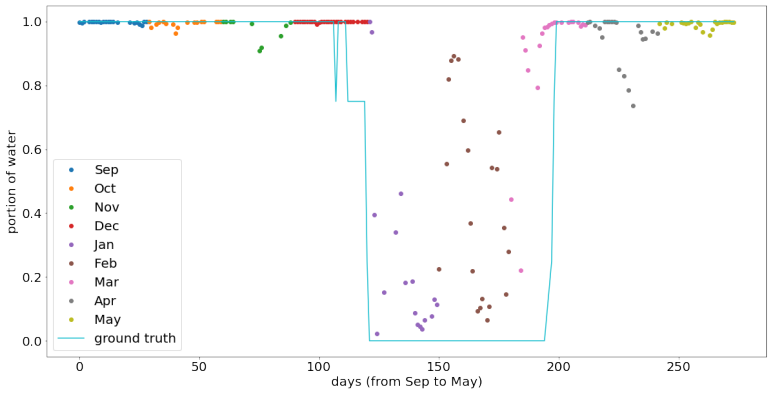

((a)) Lake Sihl in winter 2016-17

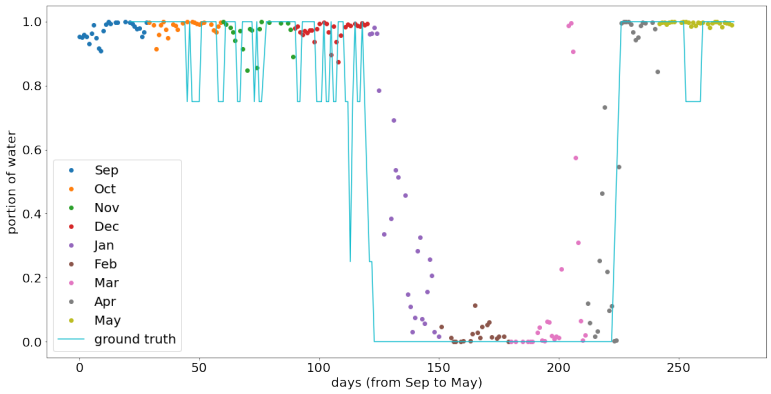

((b)) Lake Sils in winter 2016-17

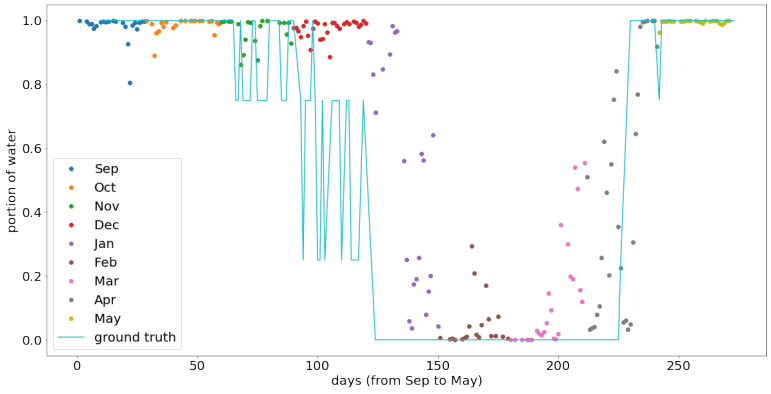

((c)) Lake Silvaplana in winter 2016-17

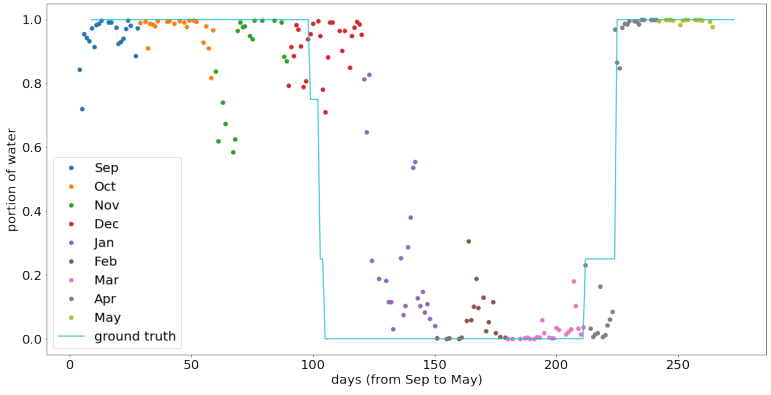

((d)) Lake St.Moritz in winter 2016-17

Figure 5.4: Time series plot of end-to-end model from leave winter 2016-17 experiment

they are two large lakes and their large amount of data can dominant the training of models. As for lake St.Moritz, the smallest lake, the performance of 2-step model is not good. For this small lake, there is no useful lake pixel in VIIRS data at all and only a few useful pixels in MODIS data. Training data of lake St.Moritz is not enough comparing to the data of other lakes. Besides, the freezing pattern of lake St.Moritz is different from others: lake St.Moritz will freeze at an earlier date and it has a longer frozen period. Thus, the lack of training data and diversity of lake freezing pattern add the difficulty of prediction.

Table 5.7: Results of ice-on and ice-off date from different methods in winter 2016-17

Date	GT	M+V[25]	Webcam[25]	2-Step	E2E
Ice-on (Sihl)	1 Jan.	3 Jan.	4 Jan.	**2 Jan.**	**2 Jan.**
Ice-off (Sihl)	14 Mar., 15 Mar.	**10 Mar.**	14 Feb.	**10 Mar.**	3 Mar.
Ice-on (Sils)	2 Jan., 5 Jan.	**6 Jan**	-	**4 Jan.**	**4 Jan.**
Ice-off (Sils)	8 Apr., 11 Apr.	31 Mar.	-	**12 Apr.**	13 Apr.
Ice-on (Silvaplana)	12 Jan.	**15 Jan.**	-	**9 Jan.**	**15 Jan.**
Ice-off (Silvaplana)	11 Apr.	30 Mar.	-	**13 Apr.**	7 Apr.
Ice-on (St.Moritz)	15-17 Dec.	1 Jan.	**14 Dec.**	2 Jan.	1 Jan.
Ice-off (St.Moritz)	30 Mar.-6 Apr.	**7 Apr.**	18 Mar-26.Apr.	12 Apr.	12 Apr.

In Table 5.7, regression tree is employed to extract ice-on and ice-off dates from the predictions of 2-step model and end-to-end model because regression tree is a good non-parametric unsupervised method which requires no prior knowledge or parameter selection. However, this is also the disadvantage of regression tree method: as there is no prior knowledge or parameter, regression tree is unconstrained and unstable. Even a small variation of data can affect the result of regression tree. The inputs of regression tree are the predictions generated by neural networks (2-step model and end-to-end), whose training involves randomness. Thus, the randomness in the training of neural network will lead to the variation of predictions, which will affect the performance of regression tree in the end.

To avoid the unstable problem of regression tree method, another decision rule with prior knowledge is tried to determine ice-on and ice-off date. After organizing predictions in Tables in Appendix A.1, a decision rule with prior knowledge is used: the day from which the water portion is lower than 25% is considered as ice-on date and the day from which the water portion is higher than 75% is considered as ice-off date. The results of ice-on and ice-off dates from 2-step predictions based regression tree method and prior knowledge method are summarized in Table 5.8. Comparing the results from two methods, their deviation is larger for ice-off date and smaller for ice-on date, which suggests our model is more certain for the prediction of ice-on date. From this comparison, it is still hard to determine which method is better, regression tree or the rule with prior knowledge. A possible improvement direction is to combine these two methods: regression tree suffers from unstable problem while prior knowledge method can add constraint to increase stability; prior knowledge method suffers from discrete predictions (for example, no acquisition for 7 and 8 of January so we do not know if the ice-on date is 6 of January of 9 of January) while regression tree can capture the general trend of predictions to overcome the discrete prediction problem.

Table 5.8: Results of ice-on and ice-off date of 2-step model using regression tree and rules with prior knowledge

Date	GT	2-Step (RT)	2-Step (prior)	deviation between 2 decision rules (days)
Ice-on (Sihl)	1 Jan.	**2 Jan.**	**2 Jan.**	0
Ice-off (Sihl)	14 Mar., 15 Mar.	10 Mar.	**17 Mar.**	7
Ice-on (Sils)	2 Jan., 5 Jan.	**4 Jan.**	**4 Jan.**	0
Ice-off (Sils)	8 Apr., 11 Apr.	**12 Apr.**	13 Apr.	1
Ice-on (Silvaplana)	12 Jan.	**9 Jan.**	6 Jan.	3
Ice-off (Silvaplana)	11 Apr.	**13 Apr.**	14 Apr.	1
Ice-on (St.Moritz)	15-17 Dec.	**2 Jan.**	**2 Jan.**	0
Ice-off (St.Moritz)	30 Mar.-6 Apr.	**12 Apr.**	21 Apr.	9

5.0.5 Miscellaneous Experiments

This part contains results and discussion of model design, further analysis of lake freezing pattern and more experiments for 2-step model.

- Model design
  Before reaching the final model design, more possibilities of models are tried. Here we will discuss the result of using Multi-Layer Perceptron (MLP) in optical-optical fusion and using Long Short-Term Memory (LSTM) as regression model in the second step of 2-Step Model.

- Analysis of ice-on and ice-off date in two winters
  To understand target lakes and chosen data, we will analyze ice-on and ice-off dates in two winters to investigate their freezing pattern. This analysis can also help understand the performance of models.

- More experiments for 2-step model
  As 2-step model achieves higher accuracy than end-to-end, more experiments are conducted for this model.

Multi-Layer Perceptron (MLP) in Optical-Optical Fusion

As MODIS and VIIRS images are small, it is natural to try models with simple structure so the first trial is using MLP. The segmentation results of using MLP to achieve optical-optical fusion are shown in Table 5.9 and Table 5.10. Comparing to the segmentation results of using CNN (Table 5.1 and Table 5.2), it is obvious that CNN is a better choice.

Table 5.9: Results of using MLP in optical-optical model on leave-one-winter experiments

Image Source	winter 16		winter 17		Average	
	accuracy	mIoU	accuracy	mIoU	accuracy	mIoU
MODIS	89.81%	77.72%	93.80%	81.61%	91.81%	79.67
VIIRS	93.14%	85.67%	93.42%	82.75%	93.28%	84.21

Table 5.10: Results of using MLP in optical-optical model on leave-one-lake experiments

Image Source	Sihl		Sils		Silvaplana		St.Moritz	
	accuracy	mIoU	accuracy	mIoU	accuracy	mIoU	accuracy	mIoU
MODIS	91.75%	72.53%	82.63%	68.59%	89.60%	80.75%	83.88%	71.55%
VIIRS	93.12%	87.11%	93.69%	88.02%	93.12%	87.11%	-	-

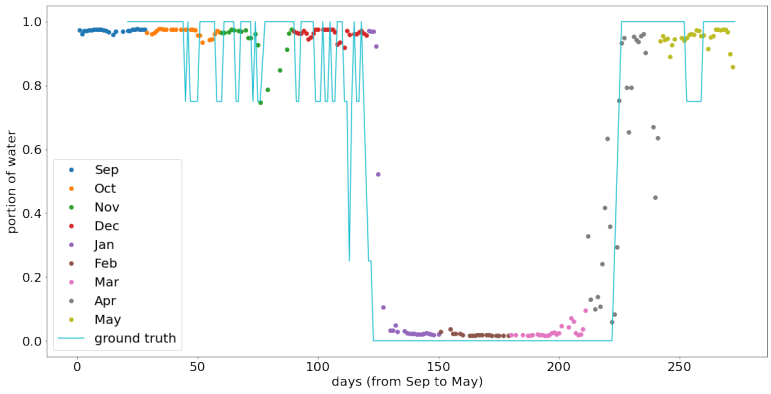

((a)) Lake Sils in winter 2016-17

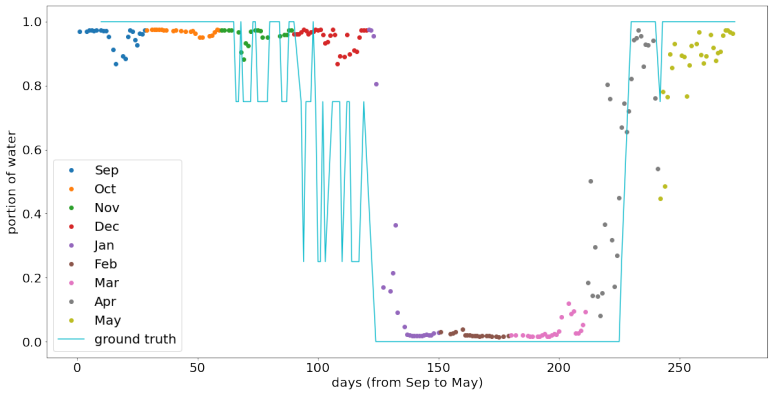

((b)) Lake Silvaplana in winter 2016-17

Figure 5.5: Time series plot of 2-step model (using LSTM) from leave winter 2016-17 experiment

Long Short-Term Memory (LSTM) in 2-Step Model

After embedding learning, we stack embedding along time dimension to leverage temporal information. A natural way to handle temporal information is using LSTM model and the resulted time series plots of lake Sils and Silvaplana are shown in Figure 5.5. There are many noisy points in plots, especially in transition period. Besides, it is normal for LSTM to encounter overfitting problem as it requires much more parameters than CNN model. Therefore, CNN is a better choice for this case.

Analysis of ice-on and ice-off date in two winters

For ground truth of ice-on and ice-off dates, they are only available for lakes in winter 2016-17. However, we can estimate the possible dates based on interpretation of per-day lake condition labels. For example, a long series of 'more snow' labels is followed by a series of 'more water' and 'water' labels. The date range of 'more water' and 'water' labels can be the possible range of ice-off date. One exception is for lake Sihl in winter 2017-18. Its freezing pattern is weird: lake is switching from water to ice, then ice to water many times so it is hard to interpret ice-on and ice-off date. To check the feasibility of this estimation method, we can estimate the dates in winter 2016-17 and compare them with given ground truth. The estimated dates and ground truth are close so this method is feasible. The estimated dates in winter 2017-18 and ground truth in winter 2016-17 are summarized in Table 5.11. By

comparing dates in two winters, it is noticed that ice-on dates are similar but ice-off dates are quite different. In general, ice-off dates in winter 2017-18 are delayed so lakes have relatively longer frozen period in this winter. The difference of ice-off dates in two winters also explains the uncertainty of ice-off date prediction when using 2-step or end-to-end model. To increase the certainty of date prediction, data in several years are required for training.

Table 5.11: Comparison of ice-on and ice-off dates in two winters

	winter 2016-17 (GT)		winter 2017-18 (Estimated)	
Lake	Ice-on date	Ice-off date	Ice-on date	Ice-off date
Sihl	1 Jan.	14 Mar., 15 Mar.	-	-
Sils	2 Jan.,	8 Apr., 11 Apr.	1 Jan.	5 May.-18 May.
Silvaplana	12 Jan.	11 Apr.	27 Dec.-1 Jan.	3 May.-5 May.
St.Moritz	15-17 Dec.	30 Mar.-6 Apr.	17 Dec.-21 Dec.	1 May.-3 May.

More experiments for 2-step model

With estimated 'ground truth' dates in winter 2017-18, we can run leave winter 2017-18 experiment for 2-step model and compare extracted dates with estimated ones. Predicted and estimated dates are shown in Table 5.12. Among those dates, the predictions of ice-off date of lake Sils and ice-on date of lake St.Moritz are worse than others. In general, the prediction in leave winter 2017-18 is worse than result in leave winter 2016-17 experiment, which indicates the instability issue of model. Because of data hungry property of deep learning method and obvious differences between freezing pattern in two winters, more training data (more than two winters) are needed for 2-step model.

Table 5.12: Ice-on and ice-off date from 2-step model in leave winter 2017-18 experiment

	2-step model		Estimated 'ground truth'	
Lake	Ice-on date	Ice-off date	Ice-on date	Ice-off date
Sihl	-	-	-	-
Sils	29 Dec.	27 Mar.	1 Jan.	5 May.-18 May.
Silvaplana	31 Dec.,	26 Apr.	27 Dec.-1 Jan.	3 May.-5 May.
St.Moritz	24 Nov.	4 May	17 Dec.-21 Dec.	1 May.-3 May.

Chapter 6

Conclusion & Discussion

Based on embedding learning, MODIS, VIIRS and Sentinel-1 SAR data are fused successfully. We achieved optical-optical and optical-SAR fusion and applied learnt embedding to determine ice-on and ice-off dates for four lakes over two winters in Switzerland. Two ideas of overall modelling, 2-step and end-to-end, are tried. The ice-on and ice-off dates resulted from 2-step model are closer to ground truth comparing to end-to-end model and previous works. The result of this work has explored the possibility to apply embedding learning idea in lake ice monitoring task. However, there are still observable limitations in this exploration work.

From experiment results, there are three remaining problems: generalisation and stability problem of models, domain gap in embedding space and selection of decision rule for date extraction. From the time series plots of 2-step model, the results of three large lakes look good while the extracted dates of lake St.Moritz are far away from ground truth. This suggests 2-step model is not generalised well for this small lake. Adjusting the model structure or increasing data size may fix this problem. Besides, embedding requires further investigation. Although the domain gap is narrowed in the visualization of embedding learnt by 2-step model, the small gap can still be observed. Exploring the embedding further may help improve the model and increase accuracy of extracted date. Right now the accuracy of model does not achieve the required accuracy. From GCOS, the accuracy requirement for ice-on and ice-off dates is ± 2 days so there is still space for improvements. The other way for improvement is making adjustment to decision rule, when extracting ice-on and ice-off date from time series plot. In this work, two decision rules, regression tree and simple rule with prior knowledge, are tried. Each of them has its own advantages and limitations so a better decision rule to combine their advantages is required.

To extend this work, more future direction can be considered. One direction is to switch from supervised to unsupervised embedding learning. As unsupervised way does not require human labelling, it is more practical in real applications. The other direction is to feed in more data sources. For example, combining MODIS, VIIRS, Sentinel-1 SAR and Sentinel-2 together in embedding learning stage. It may further improve the accuracy of date prediction. Besides, although this work only applies the idea of embedding learning in lake ice monitoring task, it is also valuable to try similar idea in other earth observation tasks.

Bibliography

[1] D. Rolnick, P. L. Donti, L. H. Kaack, K. Kochanski, A. Lacoste, K. Sankaran, A. S. Ross, N. Milojevic-Dupont, N. Jaques, A. Waldman-Brown *et al.*, "Tackling climate change with machine learning," *arXiv preprint arXiv:1906.05433*, 2019.

[2] "Essential climate variables," Feb 2019.

[3] H. H. Franssen and S. Scherrer, "Freezing of lakes on the swiss plateau in the period 1901–2006," *International Journal of Climatology: A Journal of the Royal Meteorological Society*, vol. 28, no. 4, pp. 421–433, 2008.

[4] M. Tom, R. Aguilar, P. Imhof, S. Leinss, E. Baltsavias, and K. Schindler, "Lake ice detection from sentinel-1 sar with deep learning," *arXiv preprint arXiv:2002.07040*, 2020.

[5] M. Tom, U. Kälin, M. Sütterlin, E. Baltsavias, and K. Schindler, "Lake ice detection in low-resolution optical satellite images," *International Archives of the Photogrammetry, Remote Sensing and Spatial Information Sciences*, vol. 4, no. 2, pp. 279–286, 2018.

[6] L.-C. Chen, Y. Zhu, G. Papandreou, F. Schroff, and H. Adam, "Encoder-decoder with atrous separable convolution for semantic image segmentation," in *Proceedings of the European conference on computer vision (ECCV)*, 2018, pp. 801–818.

[7] R. Latifovic and D. Pouliot, "Analysis of climate change impacts on lake ice phenology in canada using the historical satellite data record," *Remote Sensing of Environment*, vol. 106, no. 4, pp. 492–507, 2007.

[8] C. Duguay and P. Lafleur, "Determining depth and ice thickness of shallow sub-arctic lakes using space-borne optical and sar data," *International Journal of Remote Sensing*, vol. 24, no. 3, pp. 475–489, 2003.

[9] Y.-L. S. Tsai, A. Dietz, N. Oppelt, and C. Kuenzer, "Wet and dry snow detection using sentinel-1 sar data for mountainous areas with a machine learning technique," *Remote Sensing*, vol. 11, no. 8, p. 895, 2019.

[10] M. Xiao, M. Rothermel, M. Tom, S. Galliani, E. Baltsavias, and K. Schindler, "Lake ice monitoring with webcams," *International Archives of the Photogrammetry, Remote Sensing and Spatial Information Sciences*, vol. 4, no. 2, pp. 311–317, 2018.

[11] R. Prabha, M. Tom, M. Rothermel, E. Baltsavias, L. Leal-Taixe, and K. Schindler, "Lake ice monitoring with webcams and crowd-sourced images," *arXiv preprint arXiv:2002.07875*, 2020.

[12] X. Zhu, J. Chen, F. Gao, X. Chen, and J. G. Masek, "An enhanced spatial and temporal adaptive reflectance fusion model for complex heterogeneous regions," *Remote Sensing of Environment*, vol. 114, no. 11, pp. 2610–2623, 2010.

[13] X. Zhu, F. Cai, J. Tian, and T. K.-A. Williams, "Spatiotemporal fusion of multisource remote sensing data: literature survey, taxonomy, principles, applications, and future directions," *Remote Sensing*, vol. 10, no. 4, p. 527, 2018.

[14] H. Song, Q. Liu, G. Wang, R. Hang, and B. Huang, "Spatiotemporal satellite image fusion using deep convolutional neural networks," *IEEE Journal of Selected Topics in Applied Earth Observations and Remote Sensing*, vol. 11, no. 3, pp. 821–829, 2018.

[15] Q. Feng, D. Zhu, J. Yang, and B. Li, "Multisource hyperspectral and lidar data fusion for urban land-use mapping based on a modified two-branch convolutional neural network," *ISPRS International Journal of Geo-Information*, vol. 8, no. 1, p. 28, 2019.

[16] L. H. Hughes, D. Marcos, S. Lobry, D. Tuia, and M. Schmitt, "A deep learning framework for matching of sar and optical imagery," *ISPRS Journal of Photogrammetry and Remote Sensing*, vol. 169, pp. 166–179, 2020.

[17] M. Wang and W. Deng, "Deep visual domain adaptation: A survey," *Neurocomputing*, vol. 312, pp. 135–153, 2018.

[18] A. Rozantsev, M. Salzmann, and P. Fua, "Beyond sharing weights for deep domain adaptation," *IEEE transactions on pattern analysis and machine intelligence*, vol. 41, no. 4, pp. 801–814, 2018.

[19] S. Chopra, R. Hadsell, and Y. LeCun, "Learning a similarity metric discriminatively, with application to face verification," in *2005 IEEE Computer Society Conference on Computer Vision and Pattern Recognition (CVPR'05)*, vol. 1. IEEE, 2005, pp. 539–546.

[20] F. Lv, T. Liang, X. Chen, and G. Lin, "Cross-domain semantic segmentation via domain-invariant interactive relation transfer," in *Proceedings of the IEEE/CVF Conference on Computer Vision and Pattern Recognition*, 2020, pp. 4334–4343.

[21] D. P. Kingma and J. Ba, "Adam: A method for stochastic optimization," *arXiv preprint arXiv:1412.6980*, 2014.

[22] M. Sandler, A. Howard, M. Zhu, A. Zhmoginov, and L.-C. Chen, "Mobilenetv2: Inverted residuals and linear bottlenecks," in *Proceedings of the IEEE conference on computer vision and pattern recognition*, 2018, pp. 4510–4520.

[23] J. Deng, W. Dong, R. Socher, L.-J. Li, K. Li, and L. Fei-Fei, "ImageNet: A Large-Scale Hierarchical Image Database," in *CVPR09*, 2009.

[24] L. v. d. Maaten and G. Hinton, "Visualizing data using t-sne," *Journal of machine learning research*, vol. 9, no. Nov, pp. 2579–2605, 2008.

[25] M. Tom, R. Prabha, T. Wu, E. Baltsavias, L. Leal-Taixé, and K. Schindler, "Ice monitoring in swiss lakes from optical satellites and webcams using machine learning," *Remote Sensing*, vol. 12, no. 21, p. 3555, 2020.

Appendix A

Table of time series plot

A.1 Results of 2-step model

Lake Sihl, winter 2016-17

Date	Water Portion
Date	Water Portion
20160902	99.71
20160903	99.98
20160905	99.95
20160906	99.84
20160907	99.83
20160908	99.74
20160909	99.73
20160910	99.8
20160911	99.78
20160912	99.93
20160913	99.95
20160914	99.88
20160915	99.74
20160917	98.49
20160922	98.93
20160924	99.53
20160925	99.43
20160926	99.46
20160927	95.65
20160928	98.97
20160929	99.99
20160930	99.98
20161001	99.9
20161003	99.33
20161004	99.84
20161006	99.57
20161007	93.64
20161010	89.0
20161011	98.4
20161012	99.5
20161016	99.97
20161019	99.95
20161020	99.67

20161022	99.82
20161023	99.66
20161028	99.65
20161029	99.62
20161030	99.98
20161031	99.93
20161101	99.91
20161103	99.62
20161104	97.9
20161112	99.39
20161115	99.94
20161116	99.71
20161124	99.84
20161126	98.83
20161128	84.04
20161130	98.92
20161201	99.66
20161202	99.96
20161203	99.9
20161204	99.87
20161205	99.65
20161206	99.54
20161207	99.74
20161208	99.83
20161209	95.42
20161210	99.11
20161211	99.65
20161212	99.77
20161213	99.95
20161214	99.88
20161215	99.65
20161216	99.69
20161217	99.87
20161218	99.98
20161219	99.98
20161221	99.52
20161222	99.18
20161223	99.1
20161224	99.56
20161226	99.55
20161228	99.9
20161229	99.73
20161230	99.58
20161231	96.2
20170101	65.12
20170102	2.17
20170103	0.0
20170106	0.0
20170111	0.01
20170113	0.02
20170115	0.0
20170118	0.0
20170119	0.0
20170120	0.0

20170121	0.0
20170122	0.0
20170123	0.0
20170126	0.0
20170127	0.0
20170128	0.0
20170129	0.0
20170201	0.0
20170202	0.01
20170203	0.0
20170204	0.02
20170206	0.01
20170208	0.0
20170210	0.0
20170211	0.0
20170212	0.0
20170214	0.0
20170215	0.0
20170216	0.0
20170218	0.0
20170219	0.0
20170220	0.0
20170222	0.06
20170223	0.0
20170225	0.0
20170226	0.0
20170227	0.0
20170228	0.0
20170303	0.19
20170304	2.31
20170305	13.94
20170306	14.2
20170310	30.49
20170311	2.0
20170312	20.3
20170313	45.56
20170314	45.19
20170315	29.36
20170316	30.02
20170317	77.93
20170318	80.04
20170320	97.94
20170323	99.79
20170324	99.93
20170325	99.83
20170327	98.12
20170328	94.0
20170329	93.69
20170330	99.77
20170331	99.77
20170401	99.63
20170403	99.96
20170405	99.87
20170406	99.24

20170407	97.08
20170408	98.52
20170409	99.86
20170410	99.99
20170411	99.97
20170412	99.66
20170413	99.42
20170415	99.65
20170417	96.1
20170419	96.64
20170421	99.74
20170422	97.12
20170423	99.4
20170424	99.35
20170427	98.92
20170429	91.85
20170430	76.81
20170502	99.4
20170503	99.72
20170505	99.98
20170509	99.94
20170510	99.97
20170511	99.04
20170512	99.5
20170513	98.03
20170515	99.64
20170516	99.67
20170517	99.97
20170518	99.97
20170521	99.83
20170522	99.96
20170523	99.83
20170524	99.74
20170525	99.14
20170526	98.84
20170527	99.74
20170528	99.89
20170529	99.88

Lake Sils, winter 2016-17

Date	Water Portion
Date	Water Portion
20160902	97.05
20160903	97.04
20160904	93.33
20160905	93.36
20160906	97.26
20160907	98.32
20160908	98.48
20160909	98.97
20160910	98.32
20160911	99.63
20160912	99.86

20160913	99.52
20160914	99.37
20160916	99.64
20160917	99.63
20160920	94.47
20160922	98.52
20160923	98.67
20160924	99.6
20160925	99.78
20160926	99.63
20160927	99.47
20160928	99.52
20160929	99.71
20160930	99.65
20161002	97.18
20161003	98.82
20161004	99.13
20161005	99.73
20161006	99.24
20161007	98.14
20161008	98.27
20161010	99.32
20161011	99.55
20161012	98.93
20161014	98.19
20161016	99.85
20161018	99.93
20161019	99.63
20161020	99.62
20161021	99.56
20161022	99.93
20161023	91.88
20161026	22.12
20161027	54.8
20161028	66.98
20161029	98.27
20161030	99.49
20161031	99.42
20161101	99.71
20161103	99.49
20161104	97.07
20161105	98.71
20161107	96.51
20161108	83.79
20161110	95.09
20161111	93.36
20161112	92.4
20161114	92.09
20161115	71.25
20161116	90.78
20161119	83.15
20161124	69.96
20161127	97.87
20161128	98.07

20161129	95.84
20161130	96.52
20161201	97.25
20161202	94.33
20161203	86.71
20161204	95.46
20161205	93.76
20161206	93.87
20161207	98.33
20161208	98.59
20161209	99.2
20161210	99.36
20161212	99.31
20161213	99.68
20161214	99.17
20161215	98.96
20161216	98.27
20161217	99.26
20161218	96.02
20161219	92.16
20161221	89.12
20161222	98.18
20161223	98.88
20161225	98.86
20161226	98.61
20161227	98.29
20161228	99.33
20161229	99.25
20161230	97.34
20161231	95.67
20170101	94.64
20170102	95.75
20170103	45.29
20170104	7.2
20170106	0.34
20170109	0.1
20170110	0.25
20170111	1.2
20170112	0.01
20170115	0.01
20170116	0.0
20170117	0.0
20170118	0.0
20170119	0.0
20170120	0.0
20170121	0.0
20170122	0.0
20170123	0.0
20170124	0.0
20170125	0.0
20170126	0.0
20170127	0.0
20170129	0.0
20170130	0.01

20170203	0.28
20170204	0.01
20170205	0.01
20170207	0.0
20170208	0.0
20170211	0.0
20170212	0.0
20170213	0.0
20170214	0.0
20170215	0.0
20170216	0.0
20170218	0.0
20170219	0.0
20170220	0.0
20170222	0.0
20170223	0.0
20170225	0.0
20170227	0.0
20170228	0.0
20170301	0.0
20170304	0.0
20170306	0.0
20170307	0.0
20170308	0.0
20170310	0.0
20170311	0.0
20170312	0.0
20170313	0.0
20170314	0.0
20170315	0.0
20170316	0.0
20170317	0.02
20170318	0.19
20170319	0.16
20170320	0.31
20170323	0.71
20170324	0.12
20170325	0.16
20170326	0.01
20170327	0.0
20170328	0.0
20170329	0.0
20170330	0.24
20170331	8.91
20170401	0.65
20170403	0.22
20170404	0.58
20170405	1.93
20170406	11.92
20170407	14.29
20170408	12.11
20170409	10.43
20170410	0.02
20170411	1.14

20170412	28.71
20170413	82.78
20170414	95.48
20170415	98.62
20170416	52.53
20170417	18.61
20170418	2.66
20170419	10.16
20170420	49.12
20170421	92.33
20170422	97.78
20170423	94.2
20170424	92.97
20170427	49.72
20170428	67.84
20170429	50.42
20170430	88.63
20170501	96.99
20170502	89.32
20170503	89.37
20170504	92.37
20170505	98.42
20170506	94.82
20170509	98.43
20170510	99.72
20170511	98.91
20170512	91.19
20170513	98.68
20170514	98.42
20170515	98.44
20170516	99.51
20170517	97.49
20170518	98.13
20170520	96.25
20170521	98.26
20170522	99.57
20170523	99.14
20170524	97.94
20170525	99.14
20170526	98.98
20170527	99.35
20170528	99.38
20170529	96.15
20170530	99.75

Lake Silvaplana, winter 2016-17

Date	Water Portion
Date	Water Portion
20160902	99.36
20160905	99.16
20160906	99.01
20160907	99.3
20160908	94.67

20160909	92.39
20160911	99.54
20160912	99.66
20160913	99.53
20160914	99.93
20160916	99.76
20160917	89.09
20160920	62.33
20160921	90.99
20160922	88.79
20160923	99.68
20160924	99.86
20160925	99.67
20160926	93.83
20160927	99.27
20160928	99.11
20160929	99.93
20160930	99.9
20161002	99.23
20161003	99.56
20161004	99.69
20161005	99.83
20161006	99.8
20161007	99.69
20161008	99.83
20161011	99.97
20161012	99.96
20161014	100.0
20161016	100.0
20161018	100.0
20161019	99.92
20161020	99.99
20161022	99.98
20161023	99.82
20161026	95.18
20161027	98.2
20161028	96.88
20161029	99.36
20161030	99.96
20161031	99.92
20161101	99.97
20161103	99.87
20161104	99.82
20161107	98.09
20161108	50.16
20161109	85.3
20161110	55.6
20161111	96.99
20161112	98.96
20161114	80.45
20161115	97.55
20161116	97.31
20161117	99.4
20161119	97.71

20161124	82.42
20161126	94.17
20161127	98.66
20161128	99.66
20161129	98.75
20161130	99.22
20161201	96.21
20161202	97.08
20161203	97.97
20161204	99.21
20161205	98.69
20161206	96.19
20161207	98.11
20161208	99.35
20161209	99.88
20161210	99.75
20161211	99.81
20161212	99.43
20161213	90.96
20161214	96.48
20161215	97.16
20161216	98.94
20161217	99.44
20161218	88.81
20161219	82.39
20161221	87.13
20161222	99.73
20161223	98.74
20161225	93.6
20161226	90.76
20161227	97.79
20161228	99.69
20161229	99.96
20161230	99.84
20161231	99.02
20170101	99.08
20170102	98.41
20170103	72.92
20170106	10.54
20170109	1.69
20170110	0.88
20170111	3.13
20170112	0.15
20170115	0.01
20170116	0.0
20170117	0.0
20170118	0.0
20170119	0.0
20170120	0.0
20170121	0.0
20170122	0.0
20170123	0.0
20170124	0.0
20170125	0.0

20170126	0.0
20170127	0.0
20170129	0.0
20170130	0.0
20170203	0.0
20170204	0.0
20170205	0.01
20170208	0.0
20170209	0.0
20170210	0.0
20170211	0.0
20170212	0.0
20170213	0.0
20170214	0.0
20170215	0.0
20170216	0.0
20170218	0.0
20170219	0.0
20170220	0.0
20170222	0.0
20170223	0.0
20170225	0.0
20170227	0.0
20170228	0.0
20170301	0.0
20170304	0.0
20170306	0.0
20170307	0.0
20170308	0.0
20170310	0.0
20170311	0.0
20170312	0.0
20170313	0.0
20170314	0.0
20170315	0.0
20170316	0.0
20170317	0.0
20170318	0.0
20170319	0.0
20170320	0.12
20170323	0.04
20170324	0.01
20170325	0.01
20170326	0.01
20170327	0.0
20170328	0.02
20170329	0.03
20170330	0.24
20170331	0.5
20170401	3.1
20170402	0.93
20170403	3.03
20170404	0.16
20170405	0.05

20170406	0.42
20170407	12.78
20170408	52.32
20170409	58.34
20170410	2.36
20170411	0.26
20170412	1.19
20170413	30.13
20170414	91.48
20170415	99.13
20170416	98.85
20170417	94.62
20170418	67.86
20170419	92.12
20170420	85.07
20170421	99.22
20170422	99.76
20170423	96.92
20170424	99.3
20170425	98.22
20170427	79.17
20170428	92.12
20170429	44.92
20170430	52.63
20170501	97.44
20170502	74.08
20170503	97.6
20170504	99.73
20170505	99.62
20170506	99.89
20170509	98.18
20170510	99.96
20170511	99.98
20170512	99.79
20170513	99.76
20170515	99.85
20170516	99.94
20170517	81.5
20170518	39.77
20170519	70.07
20170521	87.37
20170522	99.97
20170523	99.29
20170524	92.1
20170525	94.79
20170526	96.9
20170527	99.84
20170528	99.9
20170529	99.94
20170530	99.94

Lake St.Moritz, winter 2016-17

Date	Water Portion
Date	Water Portion
20160905	97.53
20160906	96.9
20160907	90.88
20160908	83.99
20160909	77.83
20160910	96.09
20160911	95.21
20160912	98.19
20160913	97.57
20160914	97.94
20160917	96.14
20160918	97.61
20160920	97.37
20160921	95.75
20160922	97.4
20160923	97.37
20160924	89.4
20160925	59.21
20160926	50.2
20160928	13.4
20160929	82.9
20160930	68.57
20161002	47.37
20161003	70.22
20161004	97.14
20161005	90.38
20161006	97.29
20161007	71.82
20161011	20.39
20161012	37.0
20161014	67.58
20161016	88.85
20161018	95.07
20161019	95.96
20161020	90.73
20161022	97.08
20161023	95.8
20161026	98.95
20161027	98.34
20161028	99.25
20161029	99.71
20161030	99.13
20161031	97.36
20161101	91.83
20161103	92.45
20161104	91.9
20161107	88.91
20161108	97.33
20161109	95.6
20161110	99.6
20161111	97.19

20161112	97.37
20161114	97.32
20161115	97.46
20161116	93.87
20161119	90.75
20161124	93.75
20161127	47.38
20161128	69.51
20161129	60.55
20161130	70.62
20161201	90.56
20161202	93.12
20161203	97.39
20161204	94.54
20161205	86.4
20161206	88.78
20161207	75.69
20161208	95.1
20161209	87.62
20161210	93.63
20161212	76.52
20161213	88.55
20161214	87.83
20161215	97.33
20161216	93.7
20161217	93.26
20161218	92.39
20161221	62.95
20161222	50.33
20161223	16.89
20161225	29.41
20161226	19.37
20161227	82.73
20161228	55.56
20161229	80.68
20161230	77.44
20161231	81.96
20170101	79.03
20170102	19.59
20170103	2.85
20170106	0.14
20170109	0.01
20170110	0.04
20170111	0.05
20170112	0.01
20170115	1.37
20170116	0.08
20170117	0.25
20170118	0.59
20170119	0.98
20170120	7.79
20170121	0.04
20170122	0.03
20170123	0.02

20170124	0.06
20170125	0.01
20170126	0.0
20170127	0.02
20170129	0.0
20170130	0.0
20170203	0.0
20170204	0.0
20170208	0.0
20170209	0.0
20170211	0.0
20170212	0.18
20170213	0.01
20170214	0.0
20170215	0.0
20170216	0.02
20170218	0.0
20170219	0.0
20170220	0.0
20170222	0.0
20170223	0.0
20170225	0.0
20170227	0.0
20170228	0.0
20170301	0.0
20170304	0.0
20170306	0.0
20170307	0.0
20170308	0.0
20170310	0.0
20170311	0.0
20170312	0.0
20170313	0.0
20170314	0.0
20170316	0.0
20170317	0.0
20170318	0.0
20170319	0.0
20170320	0.0
20170323	0.0
20170324	0.0
20170325	0.02
20170326	0.0
20170327	0.0
20170328	0.0
20170329	0.0
20170330	0.0
20170331	0.07
20170402	0.0
20170403	0.0
20170404	0.0
20170405	0.04
20170406	0.17
20170407	0.59

20170408	1.26
20170409	0.87
20170410	1.29
20170411	0.57
20170412	49.32
20170413	76.36
20170414	92.16
20170415	61.67
20170416	13.71
20170417	18.02
20170418	17.83
20170420	8.87
20170421	74.99
20170422	94.42
20170423	93.67
20170424	92.86
20170427	97.45
20170428	98.16
20170429	97.31
20170430	80.51
20170503	96.62
20170504	87.71
20170505	79.39
20170506	69.01
20170509	89.81
20170510	93.1
20170511	98.25
20170512	96.53
20170515	98.97
20170516	98.54
20170517	79.54
20170518	18.95
20170521	67.57
20170522	91.17
20170523	87.14
20170524	59.21
20170525	83.6
20170526	92.5
20170527	99.77
20170528	99.81

A.2 Results of end-to-end model

Lake Sihl, winter 2016-17

Date	Water Portion
Date	Water Portion
20160901	96.59
20160902	97.3
20160903	98.49
20160905	97.58
20160906	97.0
20160907	99.34

20160908	98.82
20160909	97.04
20160910	97.89
20160911	99.11
20160912	98.74
20160913	98.96
20160914	97.72
20160915	97.43
20160917	96.61
20160922	97.31
20160924	97.03
20160925	98.37
20160926	94.27
20160927	92.33
20160928	98.52
20160929	99.07
20160930	97.85
20161001	95.93
20161003	96.65
20161004	98.72
20161006	99.07
20161007	99.01
20161010	92.77
20161011	95.07
20161012	96.77
20161016	98.72
20161019	97.37
20161020	96.03
20161022	97.67
20161023	98.72
20161028	98.49
20161029	98.33
20161030	98.74
20161031	99.26
20161101	99.3
20161103	98.97
20161104	98.61
20161112	93.69
20161115	94.24
20161116	87.48
20161124	86.96
20161126	94.01
20161128	97.39
20161130	97.31
20161201	99.59
20161202	99.65
20161203	99.42
20161204	98.64
20161205	98.63
20161206	98.22
20161207	99.39
20161208	97.96
20161209	97.21
20161210	97.39

20161211	98.96
20161212	99.7
20161213	99.61
20161214	98.22
20161215	98.33
20161216	99.07
20161217	99.25
20161218	99.63
20161219	99.4
20161221	98.8
20161222	97.73
20161223	96.71
20161224	96.7
20161226	99.0
20161228	99.51
20161229	97.94
20161230	98.52
20161231	98.48
20170101	90.09
20170102	49.99
20170103	20.92
20170106	29.18
20170111	76.19
20170113	78.48
20170115	63.85
20170118	51.38
20170119	33.29
20170120	33.75
20170121	31.12
20170122	33.22
20170123	31.56
20170126	15.75
20170127	34.94
20170128	41.3
20170129	40.42
20170201	76.89
20170202	78.62
20170203	79.04
20170204	92.43
20170206	89.32
20170208	52.46
20170210	84.32
20170211	65.84
20170212	60.83
20170214	36.77
20170215	35.97
20170216	49.43
20170218	27.26
20170219	57.83
20170220	76.07
20170222	83.49
20170223	52.06
20170225	58.42
20170226	50.97

20170227	53.33
20170228	75.84
20170303	83.81
20170304	82.27
20170305	88.3
20170306	87.88
20170310	84.42
20170311	92.36
20170312	95.46
20170313	96.77
20170314	95.57
20170315	94.72
20170316	95.0
20170317	96.15
20170318	98.24
20170320	95.72
20170323	97.27
20170324	96.08
20170325	98.6
20170327	98.68
20170328	95.58
20170329	95.14
20170330	97.05
20170331	99.03
20170401	98.83
20170403	96.14
20170405	95.61
20170406	93.72
20170407	96.46
20170408	98.38
20170409	98.52
20170410	98.7
20170411	98.43
20170412	98.06
20170413	92.17
20170415	78.69
20170417	85.17
20170419	62.21
20170421	93.94
20170422	97.2
20170423	92.7
20170424	92.51
20170427	87.82
20170429	89.0
20170430	96.78
20170502	96.06
20170503	96.55
20170505	96.25
20170509	94.36
20170510	96.39
20170511	93.24
20170512	98.22
20170513	92.13
20170515	97.42

20170516	96.2
20170517	97.65
20170518	96.97
20170521	94.04
20170522	96.96
20170523	99.09
20170524	96.19
20170525	97.36
20170526	96.77
20170527	98.36
20170528	98.94
20170529	98.76
20170530	98.4
20170531	97.4

Lake Sils, winter 2016-17

Date	Water Portion
Date	Water Portion
20160901	93.72
20160902	89.22
20160903	90.91
20160904	92.27
20160905	86.84
20160906	92.44
20160907	93.35
20160908	92.02
20160909	90.01
20160910	91.65
20160911	91.75
20160912	96.27
20160913	97.13
20160914	94.74
20160916	97.37
20160917	95.42
20160920	97.36
20160922	96.55
20160923	96.7
20160924	95.18
20160925	94.59
20160926	92.95
20160927	89.44
20160928	92.1
20160929	97.31
20160930	96.77
20161002	92.41
20161003	86.73
20161004	91.28
20161005	95.92
20161006	98.01
20161007	94.34
20161008	93.0
20161010	95.55
20161011	95.64

20161012	94.64
20161014	94.19
20161016	98.36
20161018	97.36
20161019	96.31
20161020	93.25
20161021	93.49
20161022	95.95
20161023	91.82
20161026	86.54
20161027	89.07
20161028	90.93
20161029	94.91
20161030	98.11
20161031	98.38
20161101	94.92
20161103	91.08
20161104	78.41
20161105	80.18
20161107	85.37
20161108	89.39
20161110	93.62
20161111	80.23
20161112	91.95
20161114	85.38
20161115	94.28
20161116	95.59
20161119	94.71
20161124	92.01
20161127	96.84
20161128	93.13
20161129	86.02
20161130	95.22
20161201	95.08
20161202	87.89
20161203	86.58
20161204	87.27
20161205	88.97
20161206	93.55
20161207	94.39
20161208	91.45
20161209	85.16
20161210	95.81
20161212	96.85
20161213	95.73
20161214	92.86
20161215	87.18
20161216	94.0
20161217	86.63
20161218	75.9
20161219	89.12
20161221	89.14
20161222	96.94
20161223	97.65

20161225	96.05
20161226	91.77
20161227	92.93
20161228	94.37
20161229	94.77
20161230	95.11
20161231	91.71
20170101	92.01
20170102	91.86
20170103	79.59
20170104	40.29
20170106	19.21
20170109	53.77
20170110	64.74
20170111	42.3
20170112	44.49
20170115	33.41
20170116	30.81
20170117	20.09
20170118	5.64
20170119	7.57
20170120	19.11
20170121	25.96
20170122	6.82
20170123	11.06
20170124	27.85
20170125	31.19
20170126	23.81
20170127	3.14
20170129	1.14
20170130	9.65
20170203	2.58
20170204	0.48
20170205	0.92
20170207	0.91
20170208	0.08
20170211	0.27
20170212	4.53
20170213	9.22
20170214	7.74
20170215	3.42
20170216	4.5
20170218	15.58
20170219	12.03
20170220	2.68
20170222	2.2
20170223	1.82
20170225	2.63
20170227	0.29
20170228	0.0
20170301	0.0
20170304	0.0
20170306	0.0
20170307	0.02

20170308	0.14
20170310	10.06
20170311	2.26
20170312	1.29
20170313	1.41
20170314	6.63
20170315	11.65
20170316	2.58
20170317	1.53
20170318	1.88
20170319	5.81
20170320	31.85
20170323	79.82
20170324	92.85
20170325	68.99
20170326	35.14
20170327	28.62
20170328	10.51
20170329	0.44
20170330	8.53
20170331	13.01
20170401	7.7
20170403	2.57
20170404	3.72
20170405	15.14
20170406	46.48
20170407	74.74
20170408	44.22
20170409	23.02
20170410	11.22
20170411	0.39
20170412	5.07
20170413	69.46
20170414	97.27
20170415	98.77
20170416	97.6
20170417	97.9
20170418	94.3
20170419	89.76
20170420	86.24
20170421	92.25
20170422	96.42
20170423	95.4
20170424	92.79
20170427	93.83
20170428	90.79
20170429	86.07
20170430	93.67
20170501	97.02
20170502	95.36
20170503	95.36
20170504	97.96
20170505	98.8
20170506	98.28

20170509	98.69
20170510	99.43
20170511	97.5
20170512	97.48
20170513	94.57
20170514	95.35
20170515	93.69
20170516	96.74
20170517	97.23
20170518	96.21
20170520	95.93
20170521	92.14
20170522	96.84
20170523	98.81
20170524	93.13
20170525	96.04
20170526	91.42
20170527	98.03
20170528	96.56
20170529	95.23
20170530	90.35

Lake Silvaplana, winter 2016-17

Date	Water Portion
Date	Water Portion
20160902	97.94
20160905	98.4
20160906	93.72
20160907	95.1
20160908	89.62
20160909	91.58
20160911	94.42
20160912	97.36
20160913	97.1
20160914	96.39
20160916	98.57
20160917	98.09
20160920	96.29
20160921	90.83
20160922	83.16
20160923	75.34
20160924	95.15
20160925	96.73
20160926	94.21
20160927	92.12
20160928	97.12
20160929	97.09
20160930	98.69
20161002	94.24
20161003	87.31
20161004	91.01
20161005	92.55
20161006	95.34

20161007	94.83
20161008	96.15
20161011	96.3
20161012	95.63
20161014	98.58
20161016	99.81
20161018	99.32
20161019	98.56
20161020	99.28
20161022	99.51
20161023	99.15
20161026	99.38
20161027	98.63
20161028	87.94
20161029	93.92
20161030	95.68
20161031	96.78
20161101	98.05
20161103	97.99
20161104	98.71
20161107	95.55
20161108	71.61
20161109	79.5
20161110	86.46
20161111	95.8
20161112	96.51
20161114	88.22
20161115	88.33
20161116	95.93
20161117	98.98
20161119	99.17
20161124	96.79
20161126	98.01
20161127	92.32
20161128	94.92
20161129	90.69
20161130	93.55
20161201	94.14
20161202	88.73
20161203	82.35
20161204	93.13
20161205	96.81
20161206	93.08
20161207	89.11
20161208	95.85
20161209	95.02
20161210	93.19
20161211	86.73
20161212	89.41
20161213	94.26
20161214	91.31
20161215	82.5
20161216	95.47
20161217	96.11

20161218	94.22
20161219	93.81
20161221	93.12
20161222	95.8
20161223	94.65
20161225	96.8
20161226	95.23
20161227	91.09
20161228	94.54
20161229	97.38
20161230	94.27
20161231	88.12
20170101	86.81
20170102	59.08
20170103	50.16
20170106	67.55
20170109	81.9
20170110	94.42
20170111	91.82
20170112	85.42
20170115	43.15
20170116	26.38
20170117	6.66
20170118	5.6
20170119	26.74
20170120	23.68
20170121	21.61
20170122	37.75
20170123	49.06
20170124	30.93
20170125	26.25
20170126	22.32
20170127	47.79
20170129	6.41
20170130	1.46
20170203	0.18
20170204	0.06
20170205	0.53
20170208	0.76
20170209	1.08
20170210	2.46
20170211	5.64
20170212	12.47
20170213	14.6
20170214	2.29
20170215	0.72
20170216	6.82
20170218	22.46
20170219	9.74
20170220	2.49
20170222	2.18
20170223	3.3
20170225	0.47
20170227	0.36

20170228	0.33
20170301	0.16
20170304	0.03
20170306	0.03
20170307	0.0
20170308	0.08
20170310	3.23
20170311	1.27
20170312	4.43
20170313	3.45
20170314	6.0
20170315	18.63
20170316	5.24
20170317	0.21
20170318	0.1
20170319	0.77
20170320	19.85
20170323	13.87
20170324	9.95
20170325	6.41
20170326	34.27
20170327	55.03
20170328	13.1
20170329	9.58
20170330	36.39
20170331	42.62
20170401	6.58
20170402	10.35
20170403	3.38
20170404	4.63
20170405	13.2
20170406	14.17
20170407	49.75
20170408	55.63
20170409	20.65
20170410	44.79
20170411	65.09
20170412	76.8
20170413	34.86
20170414	20.27
20170415	0.35
20170416	0.87
20170417	0.75
20170418	3.51
20170419	32.48
20170420	57.36
20170421	67.18
20170422	96.05
20170423	95.27
20170424	98.07
20170425	99.62
20170427	99.79
20170428	98.91
20170429	82.56

20170430	93.11
20170501	96.71
20170502	96.19
20170503	97.54
20170504	96.91
20170505	97.64
20170506	96.93
20170509	97.25
20170510	98.31
20170511	99.45
20170512	98.51
20170513	98.57
20170515	97.67
20170516	97.7
20170517	97.15
20170518	98.17
20170519	98.98
20170521	96.96
20170522	98.71
20170523	99.08
20170524	98.6
20170525	95.27
20170526	94.39
20170527	95.2
20170528	97.29
20170529	98.49

Lake St.Moritz, winter 2016-17

Date	Water Portion
Date	Water Portion
20160905	82.65
20160906	87.49
20160907	88.95
20160908	84.3
20160909	84.09
20160910	86.61
20160911	88.98
20160912	91.04
20160913	96.51
20160914	92.17
20160917	95.61
20160918	93.33
20160920	91.36
20160921	92.78
20160922	83.21
20160923	76.02
20160924	82.31
20160925	97.48
20160926	93.8
20160928	82.15
20160929	92.13
20160930	97.98
20161002	96.03

20161003	90.68
20161004	92.63
20161005	85.58
20161006	90.15
20161007	95.34
20161011	96.44
20161012	94.25
20161014	90.6
20161016	97.59
20161018	90.4
20161019	86.39
20161020	95.95
20161022	94.84
20161023	92.81
20161026	89.21
20161027	93.36
20161028	80.74
20161029	81.48
20161030	90.4
20161031	81.2
20161101	27.57
20161103	38.66
20161104	16.61
20161107	20.81
20161108	22.26
20161109	63.43
20161110	94.63
20161111	89.74
20161112	91.6
20161114	87.12
20161115	87.65
20161116	96.7
20161119	95.71
20161124	98.17
20161127	95.76
20161128	81.85
20161129	77.3
20161130	73.89
20161201	81.03
20161202	89.37
20161203	87.4
20161204	81.93
20161205	76.79
20161206	80.9
20161207	75.07
20161208	77.91
20161209	81.19
20161210	90.66
20161212	94.52
20161213	86.46
20161214	76.8
20161215	69.65
20161216	83.05
20161217	92.06

20161218	91.88
20161221	84.46
20161222	75.02
20161223	85.44
20161225	83.91
20161226	77.53
20161227	85.24
20161228	91.81
20161229	90.46
20161230	90.35
20161231	79.26
20170101	61.95
20170102	65.81
20170103	30.1
20170106	33.29
20170109	14.95
20170110	11.39
20170111	5.38
20170112	2.54
20170115	8.14
20170116	6.5
20170117	8.35
20170118	18.9
20170119	40.04
20170120	61.91
20170121	60.16
20170122	26.83
20170123	13.74
20170124	14.11
20170125	11.48
20170126	15.47
20170127	7.65
20170129	3.17
20170130	1.27
20170203	0.12
20170204	0.25
20170208	0.27
20170209	0.23
20170211	3.51
20170212	32.03
20170213	8.01
20170214	14.65
20170215	19.65
20170216	8.45
20170218	30.1
20170219	7.14
20170220	9.03
20170222	4.96
20170223	0.95
20170225	1.38
20170227	0.41
20170228	0.09
20170301	0.06
20170304	0.05

20170306	0.04
20170307	0.11
20170308	0.03
20170310	0.29
20170311	0.81
20170312	1.36
20170313	10.25
20170314	1.22
20170316	1.31
20170317	0.16
20170318	1.68
20170319	3.21
20170320	7.13
20170323	3.99
20170324	5.35
20170325	4.43
20170326	22.19
20170327	4.83
20170328	2.9
20170329	1.39
20170330	7.08
20170331	23.61
20170402	10.51
20170403	1.17
20170404	0.74
20170405	0.63
20170406	2.89
20170407	2.44
20170408	2.85
20170409	2.03
20170410	3.06
20170411	8.05
20170412	88.81
20170413	83.2
20170414	73.24
20170415	82.1
20170416	87.19
20170417	94.96
20170418	97.38
20170420	97.04
20170421	91.39
20170422	96.94
20170423	99.1
20170424	99.83
20170427	99.79
20170428	99.37
20170429	97.79
20170430	98.28
20170503	99.14
20170504	97.83
20170505	98.59
20170506	97.28
20170509	95.11
20170510	97.16

20170511	99.27
20170512	99.58
20170515	99.29
20170516	98.29
20170517	99.16
20170518	98.06
20170521	94.91
20170522	91.58